Supplementary Information for

Tunable Gap Plasmons in Gold Nanospheres Adsorbed into a pH-Responsive Polymer Film

*Chih-Yu Jao, Panupon Samaimongkol, and Hans D. Robinson**

Virginia Tech Department of Physics, Blacksburg, VA 24061

* hansr@vt.edu

S1. Multipolar scattering theory (T-matrix theory for a sphere above a metal plane)

S1.1 Introduction

We calculate the scattering off of a spherical particle separated from a solid surface by a thin film using a T-matrix[1, 2] theoretical approach, where we will largely use the notation employed by Johnson.[3] T-matrix theory is a powerful and numerically fast method for calculating the optical scattering properties of small particles and structures. In particular, it is substantially faster than techniques such as finite-difference time-domain (FDTD) or the discrete dipole approximation (DDA).[4] It also has the advantage that it generates output that is easily and accurately converted into differential and total scattering cross sections. This means for instance that extinction cross sections can be calculated with much greater ease than in alternative methods.

S1.2 T-matrix theory

In T-matrix theory, all electromagnetic waves are expanded into multipoles. For the electric field, leaving out an $e^{-i\omega t}$ factor that is common to all fields, we write

$$\mathbf{E}(\mathbf{r}) = \sum_{l=1}^{\infty}\sum_{m=-l}^{l} a_{lm}\mathbf{M}_{lm}^{(i)}(nk\mathbf{r}) + b_{lm}\mathbf{N}_{lm}^{(i)}(nk\mathbf{r}) = \begin{bmatrix} a & b \end{bmatrix}\begin{bmatrix}\mathbf{M}^{(i)}(nk\mathbf{r}) \\ \mathbf{N}^{(i)}(nk\mathbf{r})\end{bmatrix}, \tag{S1}$$

where n is the index of refraction of the medium and k is the vacuum wavenumber of the radiation. The transverse spherical vector wave functions (SVWFs) $\mathbf{M}^{(i)}$ and $\mathbf{N}^{(i)}$ can be written in terms of vector spherical harmonics (VSHs) $\mathbf{Y}_l^m(\hat{\mathbf{e}}_r)$, $\mathbf{\Psi}_l^m(\hat{\mathbf{e}}_r)$, and $\mathbf{\Phi}_l^m(\hat{\mathbf{e}}_r)$ as

$$\begin{aligned}\mathbf{M}_{lm}^{(i)}(nk\mathbf{r}) &= z_l^{(i)}(nkr)\mathbf{\Phi}_l^m(\hat{\mathbf{e}}_r), \\ \mathbf{N}_{lm}^{(i)}(nk\mathbf{r}) &= \frac{1}{nkr}\left\{\frac{\partial}{\partial r}\left[rz_l^{(i)}(nkr)\right]\mathbf{\Psi}_l^m(\hat{\mathbf{e}}_r) + \sqrt{l(l+1)}z_l^{(i)}(nkr)\mathbf{Y}_l^m(\hat{\mathbf{e}}_r)\right\}.\end{aligned} \tag{S2}$$

$z_l^{(i)}(kr)$ is a spherical bessel function, where $z_l^{(1)}(nkr) = j_l(nkr)$ for incoming waves and $z_l^{(3)}(nkr) = h_l^{(1)}(nkr)$ for outgoing waves. The VSHs in turn relate to the scalar spherical harmonics $Y_l^m(\hat{\mathbf{e}}_r)$ through

$$\begin{aligned}\mathbf{Y}_l^m(\hat{\mathbf{e}}_r) &= \hat{\mathbf{e}}_r Y_l^m, \\ \mathbf{\Psi}_l^m(\hat{\mathbf{e}}_r) &= \tfrac{1}{\sqrt{l(l+1)}}\, r\boldsymbol{\nabla} Y_l^m \quad = \tau_l^m(\theta,\varphi)\hat{\mathbf{e}}_\theta + \pi_l^m(\theta,\varphi)\hat{\mathbf{e}}_\varphi, \\ \mathbf{\Phi}_l^m(\hat{\mathbf{e}}_r) &= \tfrac{1}{\sqrt{l(l+1)}}\, \mathbf{r}\times\boldsymbol{\nabla} Y_l^m = \pi_l^m(\theta,\varphi)\hat{\mathbf{e}}_\theta - \tau_l^m(\theta,\varphi)\hat{\mathbf{e}}_\varphi,\end{aligned} \tag{S3}$$

where we have defined the auxiliary functions

$$\tau_l^m(\theta,\varphi) = \tfrac{1}{\sqrt{l(l+1)}}\frac{\partial Y_l^m(\theta,\varphi)}{\partial\theta} \;\; ; \;\; \pi_l^m(\theta,\varphi) = \tfrac{1}{\sqrt{l(l+1)}}\,\frac{im}{\sin\theta} Y_l^m(\theta,\varphi), \tag{S4}$$

and the scalar spherical harmonics have the standard normalization:

$$Y_l^m(\hat{\mathbf{e}}_r) = \sqrt{\frac{2l+1}{4\pi}\frac{(l-m)!}{(l+m)!}} P_l^m(\cos\theta\,) e^{im\varphi}\,, \tag{S5}$$

where $P_l^m(x)$ are associated Legendre polynomials. This notation also has the advantage that it separates the field into p-polarized (along $\hat{\mathbf{e}}_\theta$) and s-polarized (along $\hat{\mathbf{e}}_\varphi$) components.

The VSWFs satisfy $\mathbf{N}_{lm}^{(i)} = \frac{1}{nk}\boldsymbol{\nabla}\times\mathbf{M}_{lm}^{(i)}$ and $\mathbf{M}_{lm}^{(i)} = \frac{1}{nk}\boldsymbol{\nabla}\times\mathbf{N}_{lm}^{(i)}$ and form a complete set of solutions to Helmholtz equation. Therefore, any electromagnetic field in a charge-free medium that is consistent with Maxwell's equations can be written as a linear combination of the transverse SVWFs. Solving the scattering problem then amounts to finding the coefficients of a scattered wave

$$\mathbf{E}_S(\mathbf{r}) = [\alpha \quad \beta]\begin{bmatrix}\mathbf{M}^{(3)}(nk\mathbf{r}) \\ \mathbf{N}^{(3)}(nk\mathbf{r})\end{bmatrix} \tag{S6}$$

in terms of the coefficients of an incident wave

$$\mathbf{E}_{Inc}(\mathbf{r}) = [a \quad b]\begin{bmatrix}\mathbf{M}^{(1)}(nk\mathbf{r}) \\ \mathbf{N}^{(1)}(nk\mathbf{r})\end{bmatrix}. \tag{S7}$$

In the linear response regime, the two sets of coefficients are related by the T-matrix which gives the theory its name:

$$[\alpha \quad \beta] = [a \quad b]\begin{bmatrix}T^{11} & T^{12} \\ T^{21} & T^{22}\end{bmatrix}. \tag{S8}$$

The goal is then to find $\mathcal{T}$ for the scatterer in the problem, so that $\mathbf{E}_S$ can be found for an arbitrary $\mathbf{E}_{Inc}$. The simplest case is that of a spherical scatterer in a uniform medium, which is the well-known Mie scattering problem. This gives a fully diagonal T-matrix:

$$
\begin{aligned}
T^{11}_{lm;l'm'} &= u_l \delta_{ll'} \delta_{mm'} \,, \\
T^{22}_{lm;l'm'} &= v_l \delta_{ll'} \delta_{mm'} \,, \\
T^{12}_{lm;l'm'} &= T^{21}_{lm;l'm'} = 0 \,,
\end{aligned}
\tag{S9}
$$

where u_l and v_l are the Mie scattering coefficients:

$$
\begin{aligned}
u_l &= -\frac{n_1 \psi_l'(n_1 ka)\psi_l(n_{Sph} ka) - n_{Sph}\psi_l(n_1 ka)\psi_l'(n_{Sph} ka)}{n_1 \zeta_l'(n_1 ka)\psi_l(n_{Sph} ka) - n_{Sph}\zeta_l(n_1 ka)\psi_l'(n_{Sph} ka)}, \\
v_l &= -\frac{n_{Sph} \psi_l'(n_1 ka)\psi_l(n_{Sph} ka) - n_1\psi_l(n_1 ka)\psi_l'(n_{Sph} ka)}{n_{Sph} \zeta_l'(n_1 ka)\psi_l(n_{Sph} ka) - n_1\zeta_l(n_1 ka)\psi_l'(n_{Sph} ka)}.
\end{aligned}
\tag{S10}
$$

Here, a is the radius of the sphere, n_{Sph} and n_1 are the indices of refraction of the sphere and the embedding medium, and

$$
\psi_l(\rho) = \sqrt{\frac{\pi\rho}{2}} J_{l+\frac{1}{2}}(\rho) \quad ; \quad \zeta_l(\rho) = \sqrt{\frac{\pi\rho}{2}} H^{(1)}_{l+\frac{1}{2}}(\rho)
\tag{S11}
$$

are Riccati-Bessel functions.

A number of techniques exist for calculating the T-matrix for non-spherical particles,[5, 6] but they will not be needed in the problem at hand.

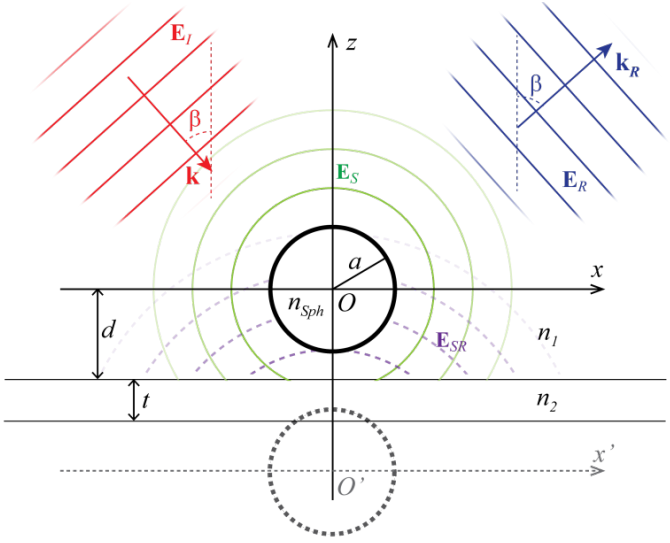

Fig. S1: Schematic of the geometry of the problem. The origin O of the coordinate system is taken at the center of the sphere, with the z-axis facing away from the substrate, so that the film surface is located at $(x, y, -d)$.

S1.3 Sphere above plane

The geometry of the situation is shown in Fig. S1, where the scattering sphere of index of refraction n_{Sph} and radius a has its center located a distance d above the top surface of a thin film with index n_2 and thickness t. The substrate below the film is taken to be semi-infinite with index of refraction n_{Sb}, and the space above the thin film is a uniform dielectric with index n_1. The origin of the default coordinate system coincides with the center of the sphere, with the z-axis pointing away from the surface, so that the top surface of the film is located at Cartesian coordinates $(x, y, -d)$.

Light is incident on the surface as a plane wave $\mathbf{E}_I$ with wave-vector in the xz-plane and angle of incidence β with respect to the z-axis. As it is reflected off the substrate, it gives rise to the reflected wave $\mathbf{E}_R$. The wave scattered from the sphere is denoted $\mathbf{E}_S$ and its reflection off the substrate as $\mathbf{E}_{SR}$. Since we are only interested in metallic substrates, we need not consider any refracted waves propagating in the lower half-space. The point O' is the center of the reflected image of the sphere in the film's top surface, and is located at $(0,0,-2d)$.

If we could ignore the substrate and the film, the problem in the figure would reduce to simple Mie scattering, with the T-matrix as specified by the diagonal matrix in Eqn. S9 (which from now on we denote $\mathcal{T}_0$). Adding back the substrate does not in principle change the nature of the scattering, but the structures of the incident and scattered fields become more complex. First, the field scattered from the surface is actually the sum of two waves

$$\mathbf{E}_{Sca} = \mathbf{E}_S + \mathbf{E}_{SR}, \tag{S12}$$

and second, the field incident on the sphere is the sum of three waves

$$\mathbf{E}_{Inc} = \mathbf{E}_I + \mathbf{E}_R + \mathbf{E}_{SR}. \tag{S13}$$

It is $\mathbf{E}_{Inc}$ and $\mathbf{E}_S$ that are related by simple Mie scattering, while the far-field problem requires us to find the T-matrix that relates $\mathbf{E}_I$ and $\mathbf{E}_{Sca}$. Finding this matrix is complicated by the fact that $\mathbf{E}_{SR}$ is part of both the incident and the scattered fields, and it is thus $\mathbf{E}_{SR}$ that accounts for the interaction between the substrate and the sphere in our treatment.

Plane waves

Even though T-matrix theory is built around multipole waves, plane waves play an important role in the problem, both because the incident wave is typically a plane wave and because reflection in the planar substrate is most easily specified for plane waves. A plane wave can be written as a superposition of SVWFs:

$$\begin{aligned} e^{in\mathbf{k}\cdot\mathbf{r}}\,\hat{\mathbf{e}}_\varphi &= \begin{bmatrix} p^{(s)} & q^{(s)} \end{bmatrix} \begin{bmatrix} \mathbf{M}^{(1)}(nk\mathbf{r}) \\ \mathbf{N}^{(1)}(nk\mathbf{r}) \end{bmatrix}, \quad \text{(s-pol.)} \\ e^{in\mathbf{k}\cdot\mathbf{r}}\,\hat{\mathbf{e}}_\theta &= \begin{bmatrix} p^{(p)} & q^{(p)} \end{bmatrix} \begin{bmatrix} \mathbf{M}^{(1)}(nk\mathbf{r}) \\ \mathbf{N}^{(1)}(nk\mathbf{r}) \end{bmatrix}, \quad \text{(p-pol.)} \end{aligned} \tag{S14}$$

where

$$\begin{aligned} p_{lm}^{(s)} &= -i^l \tau_l^m(\theta_k, -\varphi_k) \;\; ; \;\; q_{lm}^{(s)} = i^{l+1} \pi_l^m(\theta_k, -\varphi_k) \, ; \\ p_{lm}^{(p)} &= -i^l \pi_l^m(\theta_k, -\varphi_k) \;\; ; \;\; q_{lm}^{(p)} = -i^{l+1} \tau_l^m(\theta_k, -\varphi_k) \, ; \end{aligned} \tag{S15}$$

and (θ_k, φ_k) specify the direction of the wave vector $\mathbf{k}$. Next, we take advantage of the fact that it is also possible to write the SVWFs as integrals over plane waves. For incoming waves we have that

$$\begin{aligned} \mathbf{M}_{lm}^{(1)}(nk\mathbf{r}) &= \frac{i^{-l}}{4\pi} \int_0^{2\pi} d\varphi_k \int_0^{\pi} \sin\theta_k \, d\theta_k \, \mathbf{\Phi}_l^m(\hat{\mathbf{e}}_k) \, e^{in\mathbf{k}\cdot\mathbf{r}}, \\ \mathbf{N}_{lm}^{(1)}(nk\mathbf{r}) &= i \frac{i^{-l}}{4\pi} \int_0^{2\pi} d\varphi_k \int_0^{\pi} \sin\theta_k \, d\theta_k \, \mathbf{\Psi}_l^m(\hat{\mathbf{e}}_k) \, e^{in\mathbf{k}\cdot\mathbf{r}}. \end{aligned} \tag{S16}$$

For outgoing waves, building on a result by Bobbert and Vlieger[7] generalized by Fucile et al.,[8] the corresponding equations are

$$\begin{aligned} \mathbf{M}_{lm}^{(3)}(nk\mathbf{r}) &= \frac{i^{-l}}{2\pi} \int_0^{2\pi} d\varphi_k \int_{\frac{\pi}{2}+i\infty}^{\pi} \sin\theta_k \, d\theta_k \, \mathbf{\Phi}_l^m(\hat{\mathbf{e}}_k) \, e^{in\mathbf{k}\cdot\mathbf{r}}, \\ \mathbf{N}_{lm}^{(3)}(nk\mathbf{r}) &= i \frac{i^{-l}}{2\pi} \int_0^{2\pi} d\varphi_k \int_{\frac{\pi}{2}+i\infty}^{\pi} \sin\theta_k \, d\theta_k \, \mathbf{\Psi}_l^m(\hat{\mathbf{e}}_k) \, e^{in\mathbf{k}\cdot\mathbf{r}}. \end{aligned} \tag{S17}$$

Since the integrals are carried over complex wave vectors, Eq. S17 are on this form only convergent in the lower half plane, where $\mathrm{Re}(in\mathbf{k}\cdot\mathbf{r}) < 0$.

Plane waves that are reflected off of a planar surface pick up a polarization-dependent reflection coefficient $R_\sigma(\beta)$, where $\beta = \pi - \theta_k$ is the angle of incidence. In the absence of the thin film, these simply equal the Dirichlet reflectivities:

$$\begin{aligned} r_s\left(\beta, \tfrac{n_{Sb}}{n_1}\right) &= \frac{\cos\beta - \sqrt{\left(\frac{n_{Sb}}{n_1}\right)^2 - 1 + \cos^2\beta}}{\cos\beta + \sqrt{\left(\frac{n_{Sb}}{n_1}\right)^2 - 1 + \cos^2\beta}}, \\ r_p\left(\beta, \tfrac{n_{Sb}}{n_1}\right) &= \frac{\left(\frac{n_{Sb}}{n_1}\right)^2 \cos\beta - \sqrt{\left(\frac{n_{Sb}}{n_1}\right)^2 - 1 + \cos^2\beta}}{\left(\frac{n_{Sb}}{n_1}\right)^2 \cos\beta + \sqrt{\left(\frac{n_{Sb}}{n_1}\right)^2 - 1 + \cos^2\beta}} \end{aligned} \tag{S18}$$

for respectively s- and p-polarization. For non-zero thickness of the film, we have instead that

$$R_\sigma(\beta) = r_\sigma\left(\beta, \frac{n_2}{n_1}\right) + \frac{\left[1 - r_\sigma\left(\beta, \frac{n_2}{n_1}\right)\right]^2 r_\sigma\left(\beta', \frac{n_{Sb}}{n_2}\right)}{1 + r_\sigma\left(\beta, \frac{n_2}{n_1}\right) r_\sigma\left(\beta', \frac{n_{Sb}}{n_2}\right) e^{2in_2kt\cos\beta'}} e^{2in_2kt\cos\beta'}, \tag{S19}$$

where σ is either s or p, depending on the polarization of the light, and β' is the angle of refraction inside the film, given by Snell's law ($n_2 \sin\beta' = n_1 \sin\beta$).

S1.4 Finding the T matrix

To find an expression for $\mathbf{E}_{SR}$, we start from $\mathbf{E}_S$ as expressed by Eq S6. Following Fucile,[9] each of the outgoing $\mathbf{M}_{lm}^{(3)}$ and $\mathbf{N}_{lm}^{(3)}$ are then rewritten as integrals of plane waves as indicated by Eq. S17. To carry out the reflection, the integrands are first divided into s- and p-polarization components following Eq. S3. Then, each plane wave is replaced by its reflection in the film surface by taking $\mathbf{k} \to \mathbf{k_R}$ (which amounts to taking $\theta_k \to \pi - \theta_k$) and multiplying by the appropriate reflection coefficient and a phase factor that takes into account the phase lag introduced by the reflection. Specifically:

$$\begin{aligned} e^{in_1\mathbf{k}\cdot\mathbf{r}}\hat{\mathbf{e}}_\varphi &\xrightarrow{\text{reflection}} R_s(\theta_k - \pi) e^{in_1(\mathbf{k_R}\cdot\mathbf{r} - 2kd\cos\theta_k)}\hat{\mathbf{e}}_\varphi, \\ e^{in_1\mathbf{k}\cdot\mathbf{r}}\hat{\mathbf{e}}_\theta &\xrightarrow{\text{reflection}} R_p(\theta_k - \pi) e^{in_1(\mathbf{k_R}\cdot\mathbf{r} - 2kd\cos\theta_k)}\hat{\mathbf{e}}_\theta. \end{aligned} \tag{S20}$$

The reflected plane waves are then re-expressed in terms of SVWFs as in Eqs. S14 and S15 (using Einstein summation):

$$\begin{aligned} e^{in\mathbf{k_R}\cdot\mathbf{r}}\,\hat{\mathbf{e}}_\varphi &= (-1)^m\, i^{-l}\left[\tau_l^m(\theta_k, -\varphi_k),\quad i\,\pi_l^m(\theta_k, -\varphi_k)\right]\begin{bmatrix}\mathbf{M}_{lm}^{(1)}(nk\mathbf{r}) \\ \mathbf{N}_{lm}^{(1)}(nk\mathbf{r})\end{bmatrix}, \\ e^{in\mathbf{k_R}\cdot\mathbf{r}}\,\hat{\mathbf{e}}_\theta &= (-1)^m\, i^{-l}\left[-\pi_l^m(\theta_k, -\varphi_k),\quad i\,\tau_l^m(\theta_k, -\varphi_k)\right]\begin{bmatrix}\mathbf{M}_{lm}^{(1)}(nk\mathbf{r}) \\ \mathbf{N}_{lm}^{(1)}(nk\mathbf{r})\end{bmatrix}, \end{aligned} \tag{S21}$$

where we have made use of the symmetry relationships $\pi_l^m(\pi - \theta, \varphi) = (-1)^{l+m}\,\pi_l^m(\theta, \varphi)$ and $\tau_l^m(\pi - \theta, \varphi) = (-1)^{l+m+1}\,\tau_l^m(\theta, \varphi)$. Finally, we combine Eqs. S6, S17, S20, and S21 to obtain:

$$\mathbf{E}_{SR} = \begin{bmatrix}\alpha & \beta\end{bmatrix}\begin{bmatrix}F^{00} & F^{01} \\ F^{10} & F^{11}\end{bmatrix}\begin{bmatrix}\mathbf{M}^{(1)}(nk\mathbf{r}) \\ \mathbf{N}^{(1)}(nk\mathbf{r})\end{bmatrix}, \tag{S22}$$

where

$$\begin{aligned} F_{lm;l'm'}^{pq} &= F_{ll'm}^{pq} \\ &= -(-1)^m\, i^{-l-l'+p+q} \int_{\frac{\pi}{2}+i\infty}^{\pi} \sin\theta\, d\theta e^{-2in_1kd\cos\theta}\Big[(-1)^p R_s(\theta)\xi_{lm}^p(\theta)\xi_{l'm}^q(\theta) \\ &\qquad + (-1)^q R_p(\theta)\xi_{lm}^{\overline{p}}(\theta)\xi_{l'm}^{\overline{q}}(\theta)\Big] \end{aligned} \tag{S23}$$

where we are using the notation that $\tau_l^m(\theta,\varphi) = \xi_{lm}^0(\theta)e^{im\varphi}$, $\pi_l^m(\theta,0) = \xi_{lm}^1(\theta)e^{im\varphi}$, and $\begin{cases}\overline{0}=1\\ \overline{1}=0\end{cases}$. In obtaining Eq. S23, we were able to evaluate the integral over φ, which is $\int_0^{2\pi}\exp[i(m-m')\varphi] = 2\pi\delta_{m,m'}$. In other words, different values of m do not couple, so that $F^{pq}_{lm;l'm'} = 0$ unless $m' = m$. The contour integrals in Eq. S23 can be performed on the real axis by noting that they are of the form

$$\int_{\frac{\pi}{2}+i\infty}^{\pi} f(\cos\theta)\, e^{-2inkd\cos\theta}\sin\theta\, d\theta = \frac{e^{2inkd}}{2inkd}\int_0^{\infty} f\left(\frac{x}{2inkd}-1\right)e^{-x}\, dx, \tag{S24}$$

which permits numerical integration.

Since $\mathbf{E}_I$ and $\mathbf{E}_R$ are both plane waves, we will treat them as a single field:

$$\mathbf{E}_I + \mathbf{E}_R = [P \quad Q]\begin{bmatrix}\mathbf{M}^{(1)}(nk\mathbf{r})\\ \mathbf{N}^{(1)}(nk\mathbf{r})\end{bmatrix}. \tag{S25}$$

Again using Eqs. S14 and S15 and the same symmetry properties as in Eq. S21, we find that

$$\begin{aligned} P_{lm}(\beta) &= \begin{cases} i^l\tau_l^m(\beta,0)\left((-1)^{l+m} - e^{2in_1kd\cos\beta}R_s(\beta)\right), & \text{s-pol}\\ i^l\pi_l^m(\beta,0)\left(-(-1)^{l+m} - e^{2in_1kd\cos\beta}R_p(\beta)\right), & \text{p-pol}\end{cases}\\ Q_{lm}(\beta) &= \begin{cases} i^{l+1}\pi_l^m(\beta,0)\left((-1)^{l+m} + e^{2in_1kd\cos\beta}R_s(\beta)\right), & \text{s-pol}\\ i^{l+1}\tau_l^m(\beta,0)\left((-1)^{l+m} - e^{2in_1kd\cos\beta}R_p(\beta)\right), & \text{p-pol}\end{cases}\end{aligned} \tag{S26}$$

Note that we have here applied the $\pi-\theta\to\theta$ transformation to $\mathbf{E}_I$ since its wave vector has a polar angle $\theta_k = \pi-\beta$, whereas the polar angle of $\mathbf{E}_R$'s wave vector equals the angle of incidence β.

The coefficients of $\mathbf{E}_{Inc} = \mathbf{E}_I + \mathbf{E}_R + \mathbf{E}_{SR}$ can then be written as

$$[a \quad b] = [P \quad Q] + [\alpha \quad \beta]\begin{bmatrix}F^{00} & F^{01}\\ F^{10} & F^{11}\end{bmatrix}, \tag{S27}$$

which combined with Eq. S8 gives us

$$[\alpha \quad \beta]\left[\mathcal{T}_0^{-1} - \begin{bmatrix}F^{00} & F^{01}\\ F^{10} & F^{11}\end{bmatrix}\right] = [P \quad Q], \tag{S28}$$

where $\mathcal{T}_0 = \begin{bmatrix}u & 0\\ 0 & v\end{bmatrix}$ is the Mie scattering matrix given in Eqs. S9 and S10.

This means that the T-matrix can be found by matrix inversion:

$$\mathcal{T} = \left[\begin{bmatrix} u^{-1} & 0 \\ 0 & v^{-1} \end{bmatrix} - \begin{bmatrix} F^{00} & F^{01} \\ F^{10} & F^{11} \end{bmatrix}\right]^{-1}, \tag{S29}$$

which relates $\mathbf{E}_I + \mathbf{E}_R$ to $\mathbf{E}_S$. As discussed below, $\mathbf{E}_{SR}$ can then be calculated from $\mathbf{E}_S$ to find the total scattered field $\mathbf{E}_{Sca}$. The method can be adapted for other shapes by replacing $\mathcal{T}_0$ in Eq. S28 with the appropriate single particle T-matrix.

S1.5 Scattering cross sections

In the far field, outward-traveling multipole waves can be written as spherical waves modulated by a VSH:

$$\begin{aligned} \mathbf{M}_{lm}^{(3)}(nk\mathbf{r}) &\xrightarrow{r\to\infty} (-i)^l \frac{e^{inkr}}{inkr} \boldsymbol{\Phi}_l^m(\hat{\mathbf{e}}_r)\,, \\ \mathbf{N}_{lm}^{(3)}(nk\mathbf{r}) &\xrightarrow{r\to\infty} i(-i)^l \frac{e^{inkr}}{inkr} \boldsymbol{\Psi}_l^m(\hat{\mathbf{e}}_r)\,. \end{aligned} \tag{S30}$$

The scattered field $\mathbf{E}_{Sca} = \mathbf{E}_S + \mathbf{E}_{SR}$, and while $\mathbf{E}_S$ is expressed in terms of the outgoing SVWFs, our expression (Eq. S22) for $\mathbf{E}_{SR}$ is in terms of the travelling SVWFs $\mathbf{M}_{lm}^{(1)}$ and $\mathbf{N}_{lm}^{(1)}$ which do not satisfy the radiation condition at infinity, and for which Eq. S30 therefore is not valid. However, Bobbert and Vlieger[7] showed that in the far-field in direction β, $\mathbf{E}_{SR}$ can be approximated as a spherical wave originating from the mirror image of the sphere as reflected by the film surface, and modulated by the reflection coefficient $R_\sigma(\beta)$. We then obtain that in the far field

$$\mathbf{E}_{Sca}(\mathbf{r}) \xrightarrow{r\to\infty} \mathbf{F}(\hat{\mathbf{e}}_r) \cdot \frac{e^{inkr}}{inkr} = (-i)^l [\alpha \quad \beta] \begin{bmatrix} \boldsymbol{\Phi}(\hat{\mathbf{e}}_r) + \boldsymbol{\Phi}^{(\mathbf{R})}(\hat{\mathbf{e}}_r) \cdot e^{2in_1 kd\cos\beta} \\ i\boldsymbol{\Psi}(\hat{\mathbf{e}}_r) + i\boldsymbol{\Psi}^{(\mathbf{R})}(\hat{\mathbf{e}}_r) \cdot e^{2in_1 kd\cos\beta} \end{bmatrix} \cdot \frac{e^{inkr}}{inkr}. \tag{S31}$$

Fucile et al.[9] points out that this approach amounts to neglecting the effect of some fields that propagate along the surface, and offer an exact method based on mathematical translation the SVWFs. In our system, such waves are known as surface plasmon polaritons (SPPs) and can be quite important. However, the coupling to SPPs is fairly inefficient at the wavelengths around the resonances we are interested in, and also varies slowly with wavelength. For these reasons, it should have only a minor impact on the shape of the calculated extinction spectra, and accordingly we have not implemented the Fucile's more computationally costly approach here.

The experiments detailed in the paper measure the extinction of the reflected light due to absorption and scattering by the spheres located near the surface. As pointed out by Johnson,[3] the optical theorem yields that for our situation, the scattering cross section is

$$\sigma^{ext} = -\frac{4\pi}{k^2} \mathrm{Re}\{\mathbf{E}_{R0}^* \cdot \mathbf{F}(\theta = \beta, \varphi = 0)\}, \tag{S32}$$

where $\mathbf{E}_{R0}^*$ is the complex conjugate of the amplitude of the reflected plane wave $\mathbf{E}_R$, and $\mathbf{F}(\beta, 0)$ is the scattering amplitude as defined by Eq. S31, taken in the direction of propagation of $\mathbf{E}_R$.

σ^{ext} calculated in this fashion only approximates the situation in our case, as it requires that $d \geq a$, which is not true for spheres that are partially embedded in the PEM film. We are however able to carry out the calculation for the extremal cases of the sphere resting on the PEM film (corresponding to $d = a$) and the sphere being fully immersed in the film (corresponding to taking $n_1 = n_2$ and using β' as defined following Eq. S19 as the angle of incidence). As discussed in the next section, this uncertainty in index distribution leads to systematic uncertainties in our measurements of d. However, it does not generate significant relative errors, and so has little effect on our conclusions.

S2 Model validation

In this section we will detail a few additional ways we can validate our numerical model that complement the discussion in the main paper, and that will put some constraints on the film index of refraction. This in turn will allow us to better define systematic errors in the gap distances d to the extent these are due to a poorly determined film index of refraction.

The accuracy of the implementation of the model laid out in the previous section is first of all validated by Fig. 6 in the main paper, which shows good agreement between our model and both the model and experimental data presented in Ciracì et al.,[10] without invoking any adjustable parameters. However, since the films we use differ from those in that work, we still need to figure out the correct values for the indices of refractions n_1 and n_2 of the film respectively to the side of and below the gold nanospheres. In the main paper, we have chosen to take $n_2 = 1.45$, which is consistent with the index of refraction obtained by Rubner et al.,[11] which treats precisely the kind of pH-responsive films we are working with here, and with our own ellipsometry measurements. *Ciracì*, on the other hand, specifies a much higher index of refraction of 1.80 for their films. While PAH/PSS PEMs assembled at near neutral pH values should have higher index of refraction than our films, 1.80 is implausibly high, with multiple groups finding values in the range of 1.45 – 1.55, even for dried films.[12-15] But according to *Ciracì*, their high value of n_2 is required to obtain a good fit to their data. This is likely a result of the assumption that their gold particles ride on top of the films without any embedding or compression. Since d increases with n_2 for a given spectrum, such an assumption, if it is incorrect, will lead to an overestimation of n_2.

To determine appropriate indices of refraction for our film, and their consequence for the measured values of d, we will more closely examine two aspects of our data. First, we will treat the fits to the data points shown in Fig. 7 in the main paper, where gold nanospheres were deposited onto a single PAH layer that in turn was deposited on thiolated alkane acid SAMs of varying thicknesses. Second, we will examine a secondary feature visible in both our model and data, specifically a turnover in the identity of the main plasmon resonances for d values around 10 nm.

S2.1 SAM Thickness data

Since our model is quite complicated, we will here make use of an observation by Hill *et al.*[16] that the relationship between the plasmon resonance wavelength λ_{sp} and d is well modeled by a simple power law:

$$\lambda_{sp} \approx \lambda_0 \cdot d^{\alpha}, \tag{S33}$$

Figure S2 replots the contents from Fig. 7 in the main paper, with a power law fit to the average model shown in green, corresponding to $\lambda_0 = 880$ nm and $\alpha = -0.125$. Clearly, the power law fit is quite good for $d < 20$ nm, and excellent for $d < 8$ nm. This approximation allows us to characterize each theoretical calculation and data fit with just two parameters, which in turn allows us to constrain our

model by separately fitting to the experimental data in Fig. 7 (or S2) and to the weighted numerical model applied in the main paper. Note that Eq. S33 is different from the so-called plasmon ruler equation,[17, 18] and clearly is not accurate for large values of d. However, over the range under consideration here, the plasmon ruler equation is no more accurate a description of the data than Eq. S33, but is harder to use in the analysis that follows. Eq. S33 is also used in Ciracì et al.,[10] and its use here thus allows for easy comparison of our results with those in that highly relevant paper.

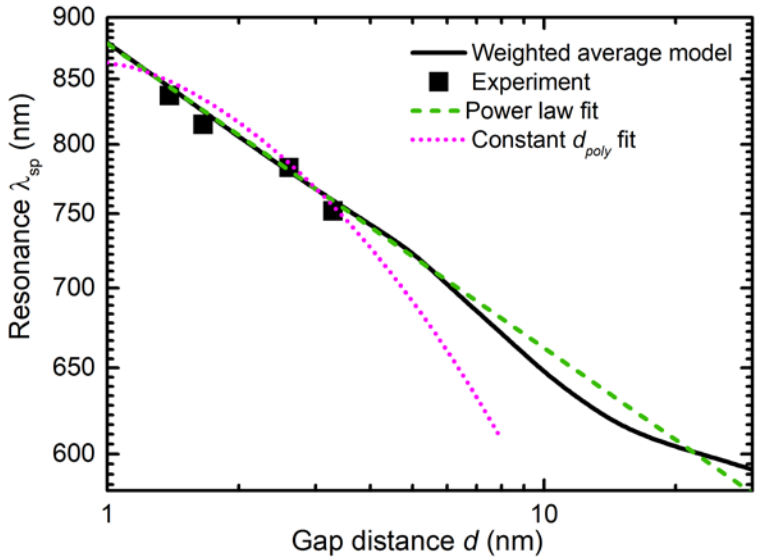

Fig. S2: Theoretical plots and experimental data for plasmon resonances in 80 nm gold nanospheres adsorbed onto a film consisting of a single monolayer of PAH on top of SAMs of varying thicknesses. The solid black line indicate the calculated plasmon resonance wavelength of the weighted numerical model used in the main paper, where it is presented in Fig. 7. The green dashed line is a power law fit to this model in the range of $d \leq 7$ nm, with $\lambda_0 = 878.5$ nm, and $\alpha = -0.1228$. The magenta dotted line represents a model obtained by requiring that $d_{aSAM} = 1.2$ nm in all cases (see section S2.3 for discussion). Experimental data is indicated with black squares, for films assembled onto charged thiol SAMs of varying thickness (3 carbons, 11 carbons, and 16 carbons) or directly on the gold surface, under the assumption that $d_{poly} = 1.5$ nm.

Turning first to the experimental data, it should be fitted to the model

$$y = \beta_0 + \alpha \ln(d_{poly} + x), \tag{S34}$$

where the dependent variable $y = \ln \lambda_{sp}$, $\beta_0 = \ln \lambda_0$, and the independent variable x is the known thicknesses of the thiol SAM films (0.0, 0.27, 1.22, and 1.9 nm). This model is nonlinear in d_{poly}, so to make progress, we take $d_{poly} = d_0 + \delta$, and expand around a best-guess value for d_0. The resulting model is

$$y = \beta_0 + \alpha \ln(d_0 + x) + \frac{\beta_1}{x + d_0} + O\left(\left(\frac{\beta_1}{x + d_0}\right)^2\right), \tag{S35}$$

where the parameter $\beta_1 = \alpha\delta$. The data can now be fit to Eq. S35 with standard linear regression. Unfortunately, over the limited range of SAM thicknesses available to us, this model is poorly conditioned, preventing us from determining all three parameters (α, β_0, and β_1) from a fit to the data. However, if we hold one parameter fixed, the two others can be determined with reasonable confidence. In other words, the best fit to the data establishes a functional relationship between the parameters, which is plotted in Figure as a solid black line in the λ_0-α plane. Each point on the line also corresponds to a specific value of d_{poly}, which is indicated by labelled ticks along the line.

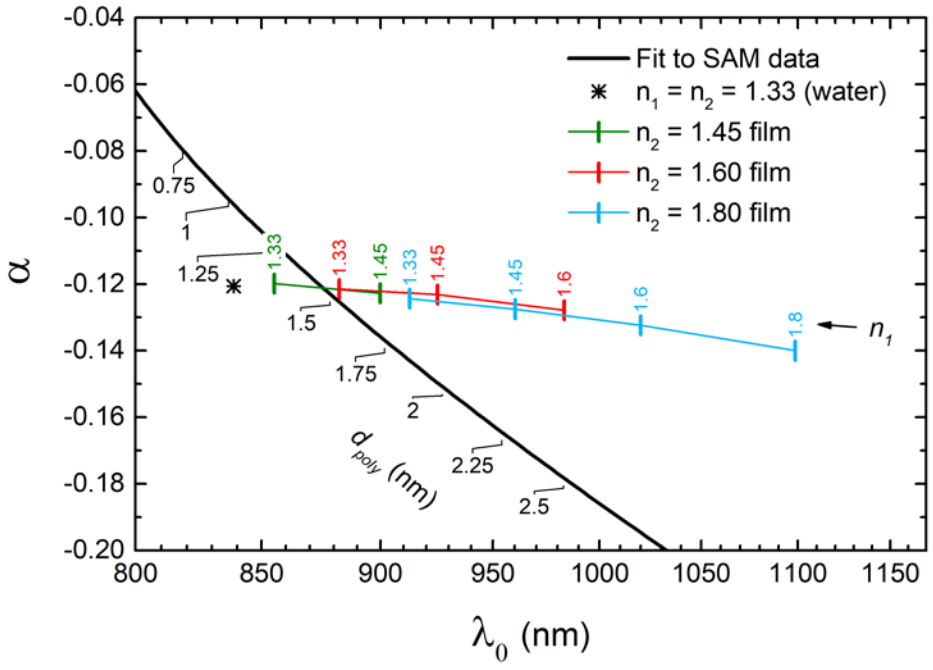

Fig. S3: Plot of best fit values of the power law parameters α and λ_0 obtained when fitting to the experimental data in Figure 7 and S2 (black solid line), and our numerical model (colored lines) under assumptions of various values of n_1 and n_2. The labelled ticks along the black line indicate the most likely values of d_{poly} for the measured films.

Turning next to our numerical model, we assume that the nanoparticle diameter equals 80 nm to good accuracy, and so keep that parameter fixed, while varying n_1 and n_2. To cover the full range of plausible indices of refraction, we ran the calculations for values of n_2 between 1.33 and 1.80, with the restriction that $1.33 \leq n_1 \leq n_2$. Each simulation run was then fit to Eq. S33, yielding the values of α and λ_0 that are plotted in Figure S3. We have restricted the fits to values of 0.7 nm $\leq d \leq$ 7 nm, both because $\lambda_{sp}(d)$ most closely follows a power law in this region, and because it corresponds to the region of the fitted experimental data.

From these fits, we can make two immediate observations about our model. First, all fits fall on or very close to a single line, even though n_1 and n_2 are two independently varied parameters. There is in other words a well-determined relationship between α and λ_0 that appears to be largely independent of the distribution of indices of refraction around the nanosphere. Second, the possible values for α fall within a narrow range between -0.120 and -0.125 for all realistic values of n_1 and n_2 applicable to our samples.

The relationship between α and λ_0 prescribed by our model can to good approximation be written as

$$\alpha(\lambda_0) \approx -0.1187 - 2.470 \cdot 10^{-5} \cdot (\lambda_0 - 800\,nm) - 1.586 \cdot 10^{-7} \cdot (\lambda_0 - 800\,nm)^2. \quad \text{(S36)}$$

Using this as a constraint on Eq. S34, the model becomes well conditioned, and we obtain that $\alpha \approx -0.1215$, $\lambda_0 \approx 876.5$ nm, and $d_{poly} \approx 1.48$ nm for the measured films. Unsurprisingly, this is very close to the intersection of the black and green curves in Figure S3, and also close to the power law parameters given in the caption of Figure S2 for the numerical model applied in the main paper. That choice of model is therefore validated by our analysis, which make only weak assumptions about the distribution of indices of refraction surrounding the nanosphere.

The 1 σ (68.3%) variance of the fit is 0.21 nm in d_{poly}, which is the parameter that interests us the most. The 2 σ (95.4%) variance is 0.92 nm, but this places the values of d_{poly} outside the limits of what is physically possible within the constraints of the model. Specifically, we know that neither n_1 nor n_2 can be less than 1.33, the index of refraction of pure water, and this slightly raises the lower bound for outside the limits of what is physically possible within the constraints of the model, to $d_{poly} = 1.50 \pm 0.90$ nm. Taking a step further, a reasonable upper bound for possible indices of refraction is $n_1 \leq 1.45$ while $n_2 \leq 1.60$, and it is highly unlikely that n_2 is any smaller than 1.39.[11] With this, we obtain that $d_{poly} = 1.5^{+0.7}_{-0.4}$ nm.

To summarize, we have that $d_{poly} = 1.48 \pm 0.21$ nm (or $\pm 14\%$) with a 68% confidence, and $d_{poly} = 1.50 \pm 0.90$ nm (or $\pm 60\%$) with 95% confidence. Taking into account our knowledge of PEM indices of refraction, the maximum errors are reduced to $^{+0.7}_{-0.4}$ nm, or $^{+46}_{-20}$ %. Since we are fitting to a power law, the same relative error (14%, 60%, etc) can be assumed for the model's full range of validity.

This is a systematic error that affects all our data. As pointed out in the main manuscript, the inaccuracy in measuring λ_{sp} is in most cases no more than about ± 5 nm or about 0.7%. From Eq. S33 we see that the relative error in our model approximately obeys $\frac{\Delta d}{d} = \frac{1}{\alpha}\frac{\Delta \lambda_{sp}}{\lambda_{sp}}$, or about 6%. In addition, inhomogeneous broadening of the plasmon peak due to variations in d within each sample may also contribute to variations in the plasmon peak position and are likely of a similar magnitude. All told, we estimate a conservative upper bound of $\pm 10\%$ random error in our data. If we compound both systematic and random error estimates, we find total errors of +48% and -23%.

S2.2 Gap plasmon anti-crossing

In addition to the plasmon resonance peak, the observed extinction spectra and our calculations both feature several secondary features. Many of these likely correspond to higher order modes and may therefore show heightened sensitivity to poorly controlled or unknown parameters, such as deviations from perfect sphericity and surface smoothness, making it hazardous to rely on them to draw conclusions about the system. However, we will here analyze one such feature—the anti-crossing behavior between two different gap plasmon modes that is seen to take place in both data and calculations for $d \sim 10$ nm—that is of first order importance to the gap distance measurement, and is fact mainly responsible for the deviations from a simple power law for $d < 20$ nm seen if Figs. 7 and S2.

In Fig. S4(a), we plot calculated extinction spectra as d is varied between 2 and 20 nm in the particle on film ($n_1 = 1.33, n_2 = 1.45$) scenario. We can see very clearly that as the nanosphere is brought closer to the surface, the main gap plasmon resonance is gradually being supplanted by a second resonance

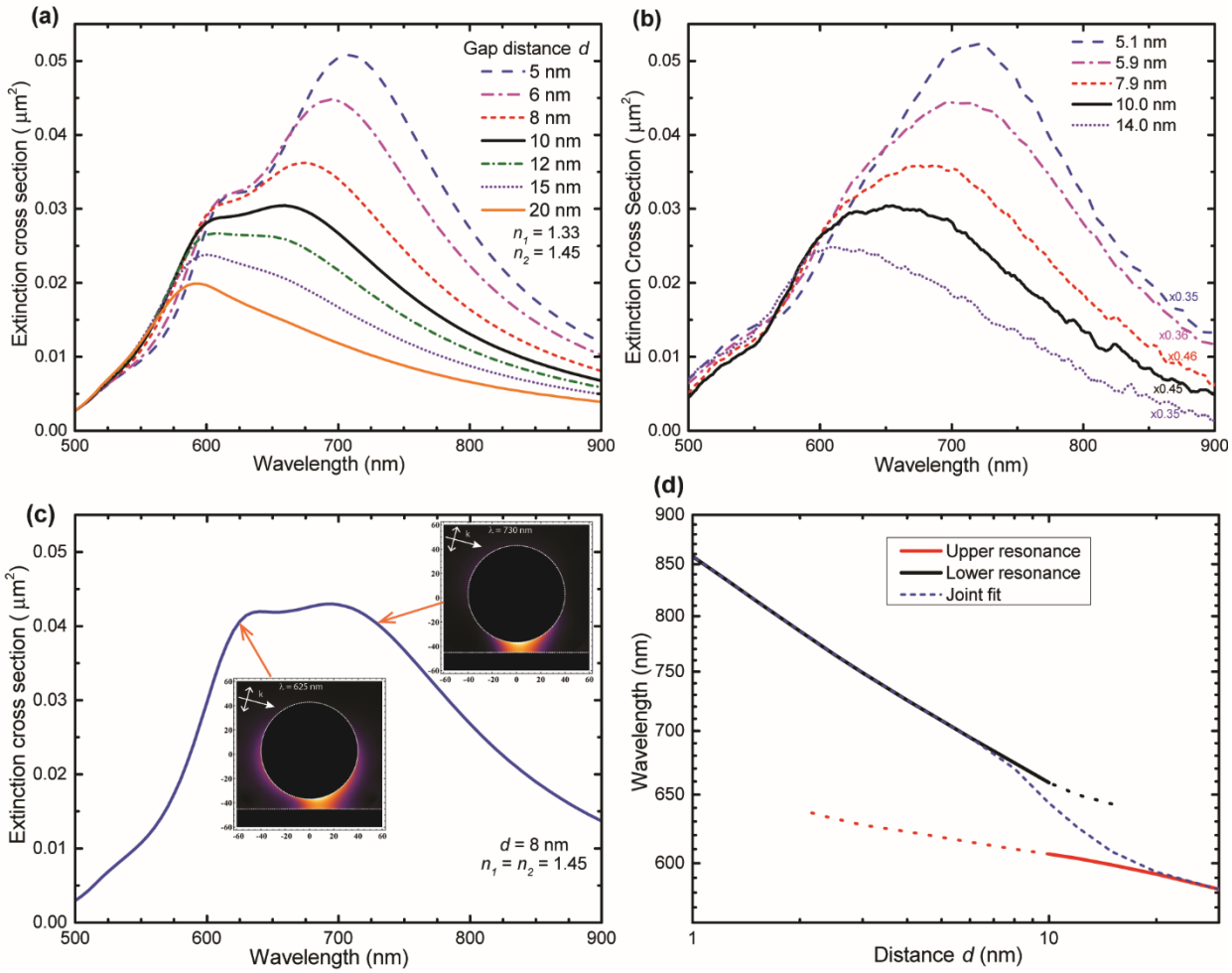

Fig. S4: (a) Calculated extinction spectra showing the anti-crossing between gap plasmon modes in a sample with $n_1 = 1.33$ and $n_2 = 1.45$. **(b)** Selected spectra of the anti-crossing region labelled by value of d derived from spectral peak positions. The spectra have been rescaled by the factors in the lower right corner of the plot. **(c)** The intensity plots show the intensity distributions for the two gap plasmon modes, calculated at the indicated wavelengths and sample conditions. **(d)** Plot of peak position for the two gap plasmon modes along with the joint fit used to model the data. The dominant mode at each value of d is plotted as a solid lines.

that emerges on its long wavelength flank, overtaking it in importance around $d \approx 10$ nm. As is shown in Fig. S4(b), the same effect is visible in the experimental data, where spectra corresponding to some of the same values d as in Fig. S4(a) are plotted for comparison. The measured spectra appear shifted somewhat to longer wavelength due to the fact that we are fitting the peak position to an average of "on film" and "in film" ($n_1 = n_2 = 1.45$) calculations, and are inhomogeneously broadened, but otherwise agree well with the calculated line shapes. The only modification we have made to these spectra is a simple scaling so that the peak height of calculated and measured spectra are the same. The scale factors used are indicated in the lower right corner of the plot in Fig. S4(b), and it is worth noting that they vary relatively little between spectra, likely reflecting a good uniformity in particle density from sample to sample. The observed anti-crossing occurs between two similar gap plasmon modes where, as shown in Fig S4(c), the bulk of the electromagnetic intensity is concentrated in the sphere-substrate gap region.

Both modes are predominantly composed of vector spherical harmonics with $m = 0$ and $|m| = 1$, but the short wavelength mode (at 625 nm in Fig. S4(c)) is dominated by $|m| = 1$ harmonics, while the longer wavelength mode is mainly made up of $m = 0$ harmonics. Since the latter are more concentrated along the vertical axis, the long wavelength gap plasmon is better able to concentrate the light within the gap, as is clear from the insets in Fig. S4(c).

In Fig S4(d), we have plotted the peak resonance position of the two gap plasmon modes vs d for the "on film" case. It is clear that power laws as in Eq. S33 are excellent models for both modes throughout the examined range. However, since noise and inhomogeneous broadening make it difficult to extract both peak positions simultaneously from the measured spectra, we have instead opted to fit the resonance to a single peak, with results in a joint fit that is indicated by the blue dashed line in Fig. S4(d). This joint fit is identical to the blue trace in Fig. 7 and results in the dip below the power law behavior evident in Fig. S2.

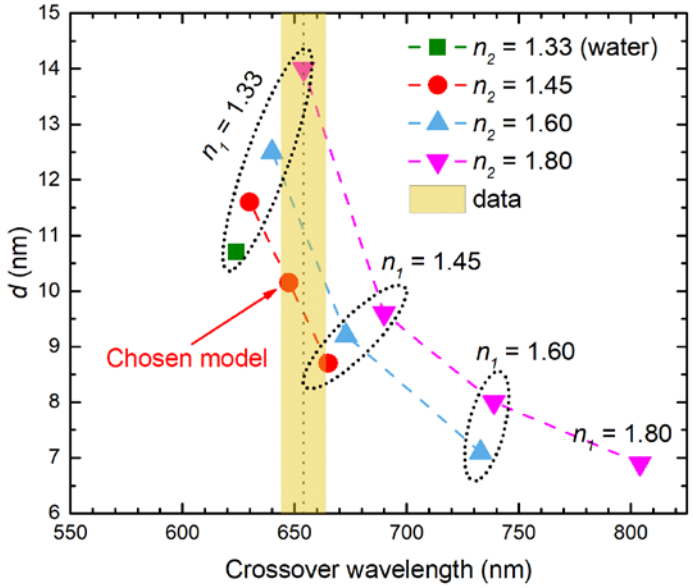

Fig. S5: Plot of d and λ_{sp} at the gap plasmon crossover point calculated at various values of $n_1$and n_2 and compared to the crossover position seen in the measured spectra.

The similarities between the calculations and data in Fig S4(a) and (b) lend further credence to our model, but we can also use the anti-crossing to provide a more quantitative validation of the calculations. This is attempted in Fig S5, where we plot the calculated values of d and λ_{sp} (calculated through a joint fit) at the point of crossover between the two modes, which we take to occur when they have the same apparent peak height in the calculated spectra. This is done for the same set of index of refraction values as were used in Fig. S2. The crossover point as it appears in the data is shown with a ±10 nm uncertainty as a beige vertical stripe. The model chosen in the paper is consistent with the observed crossover point, although so are a number of other index of refraction distributions. We can also use S5 to deduce a value of $d_{poly} = 1.75$ nm ± 30%, which is thus deduced independently of but consistent with the result found in section S2.1.

S2.3 Measuring d_{aSAM}

The plot in Fig. 15 of the main paper shows that the presence of a charged SAM below the PEM leads to an excess in polymer deposition in the films that we have designated by Category A and B. At least, that

is, if we believe our numerical model. By now, that model is fairly well validated, but it is nonetheless worthwhile to end this Supplement by pointing out what would be required of a model that confirms our naïve expectation that d_{aSAM} should equal a constant that reflects the true thickness of the free SAM monolayer, or about 1.2 nm. Since Fig. 15 indicates a fairly well-defined relationship between d_{aSAM} and the total measured d, we can in fact use our data to extract a model that conforms to the notion that $d_{aSAM} \approx 1.2$ nm. This model is plotted above in Figure S2 as a dotted magenta trace. For thinner films, the observation even under the default model in the paper is that $d_{aSAM} \approx 1.2$ nm, so in this region the two models do not differ substantially. However, for film thicknesses in excess of about 5 nm, the difference becomes large, with the constant d_{aSAM} model deviating substantially from a power law. This behavior is fundamentally in conflict with our model as well as all previously reported observations. We can therefore conclude that the excess polymer deposition we observe on the charged SAM films is real and not an artifact of an incorrect choice of modelling parameters.

1. M. I. Mishchenko, *Electromagnetic Scattering in Discrete Random Media:Fundamental Theory and Applications*, Cambridge University Press, 2002.
2. M. I. Mishchenko, G. Videen, V. A. Babenko, N. G. Khlebtsov and T. Wriedt, T-matrix theory of electromagnetic scattering by particles and its applications: a comprehensive reference database, *J. Quant. Spectros. Radia. Transfer*, 2004, **88**, 357-406.
3. B. R. Johnson, Calculation of light scattering from a spherical particle on a surface by the multipole expansion method, *J. Opt. Soc. Am. A*, 1996, **13**, 326-337.
4. J. Parsons, C. P. Burrows, J. R. Sambles and W. L. Barnes, A comparison of techniques used to simulate the scattering of electromagnetic radiation by metallic nanostructures, *Journal of Modern Optics*, 2010, **57**, 356-365.
5. M. I. Mishchenko, L. D. Travis and D. W. Mackowski, T-matrix computations of light scattering by nonspherical particles: A review, *J. Quant. Spectros. Radia. Transfer*, 1996, **55**, 535-575.
6. D. Theobald, A. Egel, G. Gomard and U. Lemmer, Plane-wave coupling formalism for T-matrix simulations of light scattering by nonspherical particles, *Phys. Rev. A*, 2017, **96**, 033822.
7. P. A. Bobbert and J. Vlieger, Light scattering by a sphere on a substrate, *Physica A*, 1986, **137**, 209-242.
8. E. Fucile, F. Borghese, P. Denti, R. Saija and O. I. Sindoni, General reflection rule for electromagnetic multipole fields on a plane interface, *Antennas and Propagation, IEEE Transactions on*, 1997, **45**, 868-875.
9. E. Fucile, P. Denti, F. Borghese, R. Saija and O. I. Sindoni, Optical properties of a sphere in the vicinity of a plane surface, *J. Opt. Soc. Am. A*, 1997, **14**, 1505-1514.
10. C. Ciracì, R. T. Hill, J. J. Mock, Y. Urzhumov, A. I. Fernández-Domínguez, S. A. Maier, J. B. Pendry, A. Chilkoti and D. R. Smith, Probing the Ultimate Limits of Plasmonic Enhancement, *Science*, 2012, **337**, 1072-1074.
11. K. Itano, J. Y. Choi and M. F. Rubner, Mechanism of the pH-induced discontinuous swelling/deswelling transitions of poly(allylamine hydrochloride)-containing polyelectrolyte multilayer films, *Macromol.*, 2005, **38**, 3450-3460.
12. Z. Feldötö, M. Lundin, S. Braesch-Andersen and E. Blomberg, Adsorption of IgG on/in a PAH/PSS multilayer film: Layer structure and cell response, *J. Colloid Interface Sci.*, 2011, **354**, 31-37.
13. J. E. Wong, F. Rehfeldt, P. Hänni, M. Tanaka and R. v. Klitzing, Swelling Behavior of Polyelectrolyte Multilayers in Saturated Water Vapor, *Macromol.*, 2004, **37**, 7285-7289.
14. H. Shibru, Y. Zhang, K. L. Cooper, G. R. Pickrell and A. Wang, Optimization of layer-by-layer electrostatic self-assembly processing parameters for optical biosensing, *Optical Engineering*, 2006, **45**, 024401.

15. N. Granqvist, H. Liang, T. Laurila, J. Sadowski, M. Yliperttula and T. Viitala, Characterizing Ultrathin and Thick Organic Layers by Surface Plasmon Resonance Three-Wavelength and Waveguide Mode Analysis, *Langmuir*, 2013, **29**, 8561-8571.
16. R. T. Hill, J. J. Mock, A. Hucknall, S. D. Wolter, N. M. Jokerst, D. R. Smith and A. Chilkoti, Plasmon Ruler with Angstrom Length Resolution, *ACS Nano*, 2012, **6**, 9237-9246.
17. A. D. Taylor, C. Lu, S. Geyer and D. L. Carroll, Thin film based plasmon nanorulers, *Appl. Phys. Lett.*, 2016, **109**, 013105.
18. P. K. Jain, W. Huang and M. A. El-Sayed, On the Universal Scaling Behavior of the Distance Decay of Plasmon Coupling in Metal Nanoparticle Pairs: A Plasmon Ruler Equation, *Nano Lett.*, 2007, **7**, 2080-2088.